Acta Pharmaceutica Sinica B 2026;16(8):5424−5438

Chinese Pharmaceutical Association
Institute of Materia Medica, Chinese Academy of Medical Sciences

Acta Pharmaceutica Sinica B

www.elsevier.com/locate/apsb
www.sciencedirect.com

ORIGINAL ARTICLE

Preclinical evaluation of a novel tetrazine probe within a pretargeted delivery system for theranostics in HER2-positive tumor-bearing mice models

Pengcheng Ma[a,†], Hui Tan[a,b,†], Qingyu Lin[a,c,†], Yuxia Liu[d], Hua Shen[d], Shuhua He[d], Hongxing Su[a], Zonghua Luo[c,e,*], Dai Shi[a,*], Dengfeng Cheng[a,c,e,*]

[a]*Department of Nuclear Medicine, Zhongshan Hospital, Fudan University, Shanghai 200032, China*
[b]*Shanghai Institute of Medical Imaging, Shanghai 200032, China*
[c]*Department of Nuclear Medicine, Shanghai Clinical Research and Trial Center, Shanghai 201210, China*
[d]*Department of Applied Chemistry, Shanghai Institute of Applied Physics, Chinese Academy of Sciences, Shanghai 201800, China*
[e]*School of Biomedical Engineering & State Key Laboratory of Advanced Medical Materials and Devices, ShanghaiTech University, Shanghai 201210, China*

Received 28 September 2025; received in revised form 11 January 2026; accepted 26 January 2026

KEY WORDS

Theranostic;
Radionuclide targeting delivery system;
Bioorthogonal click chemistry;
[^{131}I]I-Tyr-D-peptide-PEG$_{11}$-Tz;
HER2;
Nuclear medicine;
Pretargeting;

Abstract The approval of radionuclide therapy strategies in nuclear medicine has revolutionized the treatment landscape for patients with advanced malignancies. Due to significant HER2 overexpression in some solid tumors, radionuclide therapy targeting HER2 is a viable strategy. The traditional monoclonal antibody (mAb) direct radiolabelling system may lead to off-target radiation exposure. To address this limitation, we employed the established inverse-electron demand Diels-Alder (IEDDA)-based pretargeting strategy and designed a novel tetrazine probe. First, we identified the optimal targeting molecule (Pertuzumab) and optimal metabolic time (48 h) through micro-positron emission tomography/computed tomography (PET/CT) scans and biodistribution studies of [^{89}Zr]Zr-DFO-Per, [^{89}Zr]Zr-DFO-Per-F(ab')$_2$ and [^{89}Zr]Zr-DFO-Per-Fab. Next, TCO-Pertuzumab (TCO-Per) was administered to HER2-overexpressing SKOV3 tumor-bearing mice models, and after 48 h of circulation and clearance, a novel radiolabelled small molecule Tz ([^{131}I]I-Tyr-D-peptide-PEG$_{11}$-Tz) was introduced. Through a series of

*Corresponding authors.
E-mail addresses: chengdf@shanghaitech.edu.cn (Dengfeng Cheng), sdshi222@163.com (Dai Shi), luozh@shanghaitech.edu.cn (Zonghua Luo).
†These authors made equal contributions to this work.

Peer review under the responsibility of Chinese Pharmaceutical Association and Institute of Materia Medica, Chinese Academy of Medical Sciences.

https://doi.org/10.1016/j.apsb.2026.03.004

Radionuclide therapy

in vivo studies, we observed prolonged retention of [^{131}I]I-Tyr-D-peptide-PEG$_{11}$-Tz in SKOV3 tumors with rapid renal clearance, along with promising therapeutic efficacy. Our study demonstrates that the novel tetrazine probe within a pretargeting delivery system overcomes limitations of traditional strategies and shows promise for clinical translation.

1. Introduction

For the treatment of advanced solid malignancies, traditional approaches such as chemotherapy, targeted therapy, and immunotherapy have made significant progress. However, in recent years, radionuclide therapy in nuclear medicine has emerged as a promising strategy, offering more options for patients suffered from advanced tumors. Radionuclide therapy utilizes targeting molecules to deliver radioactive isotopes to tumor sites, where the emitted beta or alpha particles from radioactive decay kill the tumor cells[1].

First, appropriate target identification is essential for the development of effective theranostic strategies. Human epidermal growth factor receptor 2 (HER2), a member of the tyrosine kinase receptor family, is markedly overexpressed in a wide range of solid tumors, including breast cancer, gastric and gastro-oesophageal junction cancers, biliary tract cancer, colorectal cancer, non-small-cell lung cancer, and bladder cancer[2,3]. In the clinic, HER2-targeted monoclonal antibodies, such as trastuzumab and pertuzumab, have achieved substantial therapeutic success and significantly improved the prognosis of patients with HER2-positive malignancies. Building upon this foundation, antibody−drug conjugates (ADCs), including trastuzumab emtansine (T-DM1) and trastuzumab deruxtecan (T-DXd), have further expanded therapeutic options and demonstrated encouraging clinical outcomes across multiple tumor types[4,5]. Nevertheless, despite these advances, HER2-targeted ADCs remain limited by the emergence of resistance mechanisms and treatment-related toxicities. Beyond ADCs, nuclear medicine has explored monoclonal antibodies as carriers for the targeted delivery of diagnostic and therapeutic radionuclides, leveraging their high specificity and affinity for HER2. For diagnostic imaging, several HER2-targeted PET probes, such as [^{64}Cu]Cu-DOTA-trastuzumab[6,7] and [^{89}Zr]Zr-trastuzumab[8,9], are currently under clinical investigation. For therapy, HER2-targeted radioimmunotherapy (RIT) using radiolabelled monoclonal antibodies, including [^{67}Cu]Cu-Sar-trastuzumab, [^{225}Ac]Ac-DOTA-trastuzumab, [^{177}Lu]Lu-DOTA-pertuzumab, and [^{90}Y]Y-anti-HER2, has demonstrated promising antitumor efficacy in preclinical and early clinical studies[10-12]. However, the slow clearance and prolonged circulation half-life of radiolabelled antibodies often result in high background activity, elevated blood-pool retention, and increased radiation exposure to radiosensitive organs such as the bone marrow, lungs, and liver. These limitations raise safety concerns and substantially hinder the broader clinical translation of HER2-targeted radioimmunotherapy, underscoring the need for alternative strategies to improve imaging contrast and therapeutic safety.

Therefore, in this study, we aimed to develop a radionuclide targeting delivery system for HER2 that overcomes the inherent limitations of direct antibody labelling. This radionuclide delivery system is designed based on the IEDDA reaction, leveraging the near-instantaneous click chemistry between *trans*-cyclooctene (TCO) and tetrazine (Tz) to form a stable six-membered ring structure. TCO is conjugated to monoclonal antibody (mAb) or mAb fragments to form a lead molecule, which is allowed to circulate and metabolize *in vivo* without any radiation dose. After the lead molecule has cleared from non-target organs, a radiolabelled small molecule Tz is introduced to "click" with the lead molecule specifically bound to the tumor site.

The overall workflow of this study is illustrated in Graphical abstract. In this study, in addition to Per (an FDA-approved anti-HER2 mAb) was used, we prepared two more lead molecules, Per-F(ab')$_2$ and Per-Fab, through enzymatic digestion. To screen for the optimal lead molecule, we prepared three ^{89}Zr-labelled molecular probes ([^{89}Zr]Zr-DFO-Per, [^{89}Zr]Zr-DFO-Per-F(ab')$_2$ and [^{89}Zr]Zr-DFO-Per-Fab) and validated them using micro-PET/CT in tumor-bearing mice models. After evaluating and analyzed by the results of PET imaging, TCO-Per was chosen as the lead molecule of our radionuclide targeting delivery system. For the radiolabelled Tz, the [^{131}I]I-Tyr-D-peptide-PEG$_{11}$-Tz with excellent biochemical properties was synthesized. Ultimately, the radionuclide targeting delivery system (TCO-Per and [^{131}I]I-Tyr-D-peptide-PEG$_{11}$-Tz) was evaluated in tumor-bearing mice models, and its therapeutic efficacy was further assessed.

2. Materials and methods

2.1. Cell lines

The HER2-positive ovarian SKOV3 and HER2-negative gastric MGC-803 human cancer cell lines were purchased from Shanghai Zhong Qiao Xin Zhou Biotechnology (Shanghai, China). SKOV3 and MGC-803 cells were maintained at 37 °C in a humidified atmosphere at 5% CO_2 in RPMI-1640 growth medium supplemented with 10% foetal bovine serum and 1% concentrations of both penicillin and streptomycin.

2.2. Animal model establishment

All animal studies followed protocols approved by the Animal Ethics Committee of Zhongshan Hospital, Fudan University. Six-week-old male NU/NU mice were purchased from Beijing Vital River Laboratory Animal Technology (Beijing, China). Subcutaneous tumor cells (SKOV3 and MGC-803 cells) were induced in the mice by injecting their lower right flank with 5×10^5 cells suspended in 200 μL of 0.01 mol/L phosphate-buffered saline

(PBS). After the volumes of the subcutaneous tumors reached 800−1000 mm^3, the following studies were conducted.

2.3. Western blotting (WB)

SKOV3 and MGC-803 cells were lysed using radioimmunoprecipitation assay (RIPA) lysis buffer containing protease and phosphatase inhibitors at 4 °C for 30 min. After centrifugation at 13,000×*g* for 10 min at 4 °C, the supernatants were denatured with protein loading buffer at 100 °C for 10 min. The processed samples were then loaded into the gel wells. The proteins were electrophorized for 90 min at 100 V and transferred to a polyvinylidene fluoride (PVDF) membrane. The PVDF membrane was subsequently incubated with HER2 primary antibodies and β-actin primary antibodies overnight at 4 °C after being blocked with 5% skim milk blocking buffer for 2 h at 20 °C. After being washed three times with TBS-Tween 20, the PVDF membrane was incubated with a goat anti-rabbit secondary antibody at 20 °C for 1 h. The washed membrane was scanned and quantitatively analysed using a Tanon 4200 imaging system (Tanon, Shanghai, China). Furthermore, HER2 expression was analysed and normalized to β-actin protein expression for comparison using ImageJ 1.44p (National Institutes of Health, Bethesda, MA, USA).

2.4. Preparation of Cy3-Per

Per was conjugated with cyanine 3 *N*-hydroxysuccinimide ester (Cy3-NHS ester) for 2 h at a 1:5 M ratio of Per to Cy3-NHS ester in 0.1 mol/L carbonate buffer (pH 9.0). The fluorescence product was purified using PD-10 columns to remove excess Cy3-NHS ester.

2.5. Immunocytochemistry (ICC)

SKOV3/MGC-803 cells were cultured in six-well plates to 40% confluence and then incubated with 66.67 nmol/L Cy3-Per overnight. Images were captured using an Olympus imaging system (Olympus, Tokyo, Japan).

2.6. Flow cytometry

HER2 expression on the cell surfaces of the SKOV3 and MGC-803 cell lines was evaluated using flow cytometry analysis. The resuspended cells were incubated with CY3-Per or an isotype control CY3-IgG at 20 °C for 60 min. Flow cytometry analysis was performed on a flow cytometer (BD, Heidelberg, Germany), and the data were processed using Flow Jo software version 10.8.0 (Flow Jo, Ashland, USA).

2.7. Preparation of the Per-F(ab')$_2$ and Per-Fab fragments

The synthesis procedures for Per-F(ab')$_2$ and Per-Fab are based on our previous research[13]. The quality control of Per, Per-F(ab')$_2$ and Per-Fab was then analysed using sodium dodecyl sulphate-polyacrylamide gel electrophoresis (SDS-PAGE) and size-exclusion chromatography-high-performance liquid chromatography (SEC-HPLC).

2.8. ^{89}Zr radiolabelling and binding assays

Radiolabelling with Zr-89 was achieved using the multifunctional chelator *p*-SCN-Bn-DFO (*p*-SCN-Bn-deferoxamine). Per, Per-F(ab')$_2$ and Per-Fab were dissolved in 0.1 mol/L sodium bicarbonate buffer (pH 9.0) at a final concentration of at least 1 mg/mL *p*-SCN-Bn-DFO was dissolved in DMSO (dimethyl sulfoxide) at a final concentration of 5 mg/mL. The mixture was prepared according to a 1:10 M ratio of Per, Per-F(ab')$_2$ and Per-Fab to *p*-SCN-Bn-DFO, and the reaction was performed at 4 °C for 10 h. DFO-Per, DFO-Per-F(ab')$_2$ and DFO-Per-Fab were purified using a PD-10 desalting column with 0.5 mol/L HEPES (4-(2-hydroxyethyl)-1-piperazineethanesulfonic acid) as the elution buffer, and subsequently subjected to liquid chromatography-mass spectrometry (LC−MS) analysis for quality control. [^{89}Zr]ZrC_2O_4 was purchased from Nanjing PET-Tracer (DC AMS PHARMA, Nanjing, China). For radiolabelling, a mixture of 200 μL of DFO-Per, DFO-Per-F(ab')$_2$ or DFO-Per-Fab (0.67 nmol) in 0.5 mol/L HEPES and 100 μL of [^{89}Zr]ZrC_2O_4 (37 MBq) was incubated at 20 °C for 30 min. After purification using a PD-10 desalting column with 0.01 mol/L PBS as the elution buffer, [^{89}Zr]Zr-DFO-Per, [^{89}Zr]Zr-DFO-Per-F(ab')$_2$ and [^{89}Zr]Zr-DFO-Per-Fab were obtained. The radiochemical purities of [^{89}Zr]Zr-DFO-Per, [^{89}Zr]Zr-DFO-Per-F(ab')$_2$ and [^{89}Zr]Zr-DFO-Per-Fab were determined using radio-thin layer chromatography (LabLogic, Sainfield, UK) using 20 mmol/L sodium citrate buffer as the mobile solvent.

A 96-well plate coated with 100 ng of human HER2 antigen was used for the binding assays. After 2 h of blocking with 4% BSA, different concentrations of [^{89}Zr]Zr-DFO-Per, [^{89}Zr]Zr-DFO-Per-F(ab')$_2$ and [^{89}Zr]Zr-DFO-Per-Fab were added to the wells. After incubation at 37 °C for 1 h, the samples were washed three times with phosphate-buffered saline containing Tween 20 (PBST), and the radioactive count of each well was measured.

2.9. [^{89}Zr]Zr-DFO-Per, [^{89}Zr]Zr-DFO-Per-F(ab')$_2$ and [^{89}Zr]Zr-DFO-Per-Fab PET imaging of tumor-bearing mouse models and biodistribution studies of [^{89}Zr]Zr-DFO-Per

For PET/CT imaging, [^{89}Zr]Zr-DFO-Per, [^{89}Zr]Zr-DFO-Per-F(ab')$_2$ and [^{89}Zr]Zr-DFO-Per-Fab PET imaging of tumor-bearing mouse models was conducted on a Nano PET/CT scanner (uBiomicro PET/CT, United Imaging, China). A total of 12 SKOV3 tumor-bearing models and 3 MGC-803 tumor-bearing models were divided into five groups: Group A (SKOV3 tumor-bearing mice that were injected with 1.85 MBq [^{89}Zr]Zr-DFO-Per), Group B (SKOV3 tumor-bearing mice that were injected with 1.85 MBq [^{89}Zr]Zr-DFO-Per-F(ab')$_2$), Group C (SKOV3 tumor-bearing mice that were injected with 1.85 MBq [^{89}Zr]Zr-DFO-Per-Fab), the Blocking group (SKOV3 tumor-bearing mice injecting unlabelled 0.3 mg Per before that were injected with 0.85 MBq [^{89}Zr]Zr-DFO-Per), and the Negative control group (MGC-803 tumor-bearing mice that were injected with 1.85 MBq [^{89}Zr]Zr-DFO-Per). Before the PET scan, a 5-min CT whole-body scan was conducted for anatomical coregistration. For CT images, attenuation correction in CT (ACCT) scanning was conducted with the following scan parameters: a current of 200 μA, a rotation angle of 2146°, and a pitch of 1. The reconstruction was performed with parameters of 219.3-μm pixel dimensions and a 456 matrix using the manufacturer's software. PET was performed after CT scanning with the same bed position for 20 min. The PET images were reconstructed using the OSEM-3D algorithm, and

image corrections were performed using scatter correction, registration matrix adjustment, and ACCT. Following CT and PET data reconstruction, the DICOM files were imported into the fusion module of PMOD software (v4.1; PMOD Technologies Ltd., Zurich, Switzerland).

For biodistribution assay, the tumor-bearing mice were killed and dissected following the injection with tracers for 6, 24, 48, 72 and 120 h. Tumors, blood, heart, lung, liver, kidney, spleen, colon, stomach, and muscles were harvested and weighed, and radioactivity counts were measured. Tissue radioactivity is expressed as the percentage injected activity per gram (%IA/g).

2.10. *Preparation of TCO-Per*

Per was dissolved in 0.1 mol/L sodium bicarbonate buffer (pH 9.0) at a final concentration of at least 1 mg/mL. The *trans*-cyclooctene *N*-hydroxysuccinimide ester (TCO-NHS ester) was dissolved in DMSO at a final concentration of 5 mg/mL. The mixture was prepared according to a 1:50 M ratio of Per to TCO-NHS ester, and the reaction was performed at 4 °C for 10 h at pH 8.8-9 (Supporting Information Fig. S1A). TCO-Per was purified using a PD-10 desalting column with 0.01 mol/L PBS as the elution buffer.

2.11. *Synthesis of the radiolabelled precursor Tyr-D-peptide-PEG$_{11}$-Tz*

The complete synthetic route of Tyr-D-peptide-PEG$_{11}$-Tz was illustrated in Fig. 1A, with detailed synthetic procedures provided in the Supporting Information (Supporting Information Fig. S2−S16, Tables S1 and S2). As shown in Fig. 1B, the molecule consists of three key components highlighted in distinct colors: the red region represents the tetrazine group, which is used for click reactions with TCO-modified antibodies (TCO-mAb); the blue region corresponds to hydrophilic modifications provided by polyethylene glycol (PEG) and D-polypeptide sequence (Gly-Arg-Glu-Arg-Glu-Lys); and the green region indicates the tyrosine group, which serves as a linker for radionuclide labelling.

2.12. *^{131}I radiolabelling*

Na^{131}I was purchased from Shanghai Atom Kexing Pharmaceuticals (Shanghai, China). For iodogen tube preparation, iodogen was dissolved in dichloromethane to a final concentration of 1 mg/mL. Then, 50 μg of iodogen was added to the bottom of the glass tube and dried using nitrogen while rotating at a constant speed such that the iodogen was evenly distributed at the bottom of the tube. For radiolabelling, 60 μg of Tyr-D-peptide-PEG$_{11}$-Tz in 0.01 mol/L PBS and 105-120 MBq Na^{131}I solution were added to an iodogen tube. The reaction occurred at 20 °C for 15 min [^{131}I]I-Tyr-D-peptide-PEG$_{11}$-Tz was purified by pre-HPLC.

2.13. *In vitro and in vivo stability, distribution coefficient, specificity, and binding assays*

The *in vitro* stability of [^{131}I]I-Tyr-D-peptide-PEG$_{11}$-Tz was evaluated in 0.01 mol/L PBS and 10% fetal bovine serum (FBS). [^{131}I]I-Tyr-D-peptide-PEG$_{11}$-Tz (2 μL) was added to 48 μL of

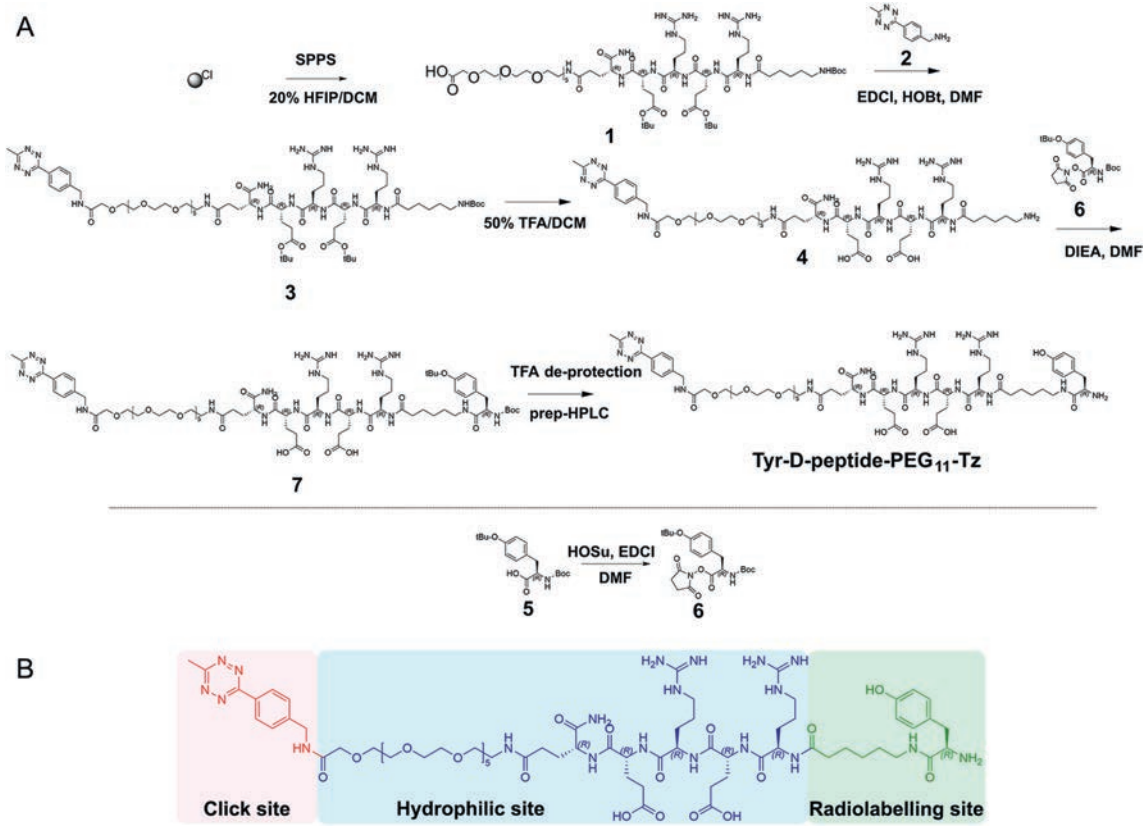

Figure 1 Synthesis route and structural formula of Tyr-D-peptide-PEG$_{11}$-Tz. (A) Synthesis route of Tyr-D-peptide-PEG$_{11}$-Tz. (B) The structural formula of Tyr-D-peptide-PEG$_{11}$-Tz.

0.01 mol/L PBS or 10% FBS and incubated at 20 °C for 0, 6, 24, 48, 72, 96, or 120 h. Radiochemical purity was determined by paper chromatography at each time point using 20 mmol/L sodium citrate buffer as the mobile solvent. For the *in vivo* stability assay, [^{131}I]I-Tyr-D-peptide-PEG$_{11}$-Tz was administered to mice *via* tail vein injection, and blood samples were collected at predetermined time points (6, 12, and 24 h). Radiochemical purity was assessed at each time point by paper chromatography using 20 mmol/L sodium citrate buffer as the mobile phase.

For the distribution coefficient assay, 500 μL of *n*-octanol, 500 μL of water, and 10 μL of [^{131}I]I-Tyr-D-peptide-PEG$_{11}$-Tz were added sequentially to a 1.5-mL EP tube. The tube was sealed and shaken vigorously at 20 °C for 10 min. After centrifugation using a Thermo Scientifi Micro 17 microcentrifuge (Thermo Fisher Scientific, Waltham, MA, North America, USA) at 12,000 rpm for 5 min at 20 °C, the CPM (counts per min) of equal volumes of the *n*-octanol and aqueous phases were measured. The log*D* value was then calculated using the following formula: log*D* = log (*n*-octanol count/aqueous phase count).

A 96-well plate coated with 100 ng of human HER2 antigen was used for both the specificity and binding assays. For the specificity assay, the experiment was divided into five groups: A, B, C, D, and E. Group A contained TCO-Per (100 nmol/L) and [^{131}I]I-Tyr-D-peptide-PEG$_{11}$-Tz (1.85×10^5 Bq). Group B contained Per (100 nmol/L) and [^{131}I]I-Tyr-D-peptide-PEG$_{11}$-Tz (1.85×10^5 Bq). Group C contained [^{131}I]I-Tyr-D-peptide-PEG$_{11}$-Tz (1.85×10^5 Bq). Group D contained Per (10 mmol/L), TCO-Per (100 nmol/L), and [^{131}I]I-Tyr-D-peptide-PEG$_{11}$-Tz (1.85×10^5 Bq). Group E contained TCO-IgG (100 nmol/L) and [^{131}I]I-Tyr-D-peptide-PEG$_{11}$-Tz (1.85×10^5 Bq). After 1 h of incubation, the wells were washed three times with 0.01 mol/L PBS, and the CPS counts was measured. Each group was tested in triplicate, and the experiment was repeated three times. For the binding assay, the click chemistry reactions for TCO-Per and [^{131}I]I-Tyr-D-peptide-PEG$_{11}$-Tz were performed *in vitro* to generate [^{131}I]I-Tyr-D-peptide-PEG$_{11}$-Tz-TCO-Per before the experiment. After 2 h of blocking with 4% BSA, different concentrations of [^{131}I]I-Tyr-D-peptide-PEG$_{11}$-Tz-TCO-Per (1.17−150 nmol/L) were added to the wells. After incubation at 37 °C for 1 h, the samples were washed three times with phosphate-buffered saline containing Tween 20 (PBST), and the radioactive count of each well was measured.

2.14. Pharmacokinetic assays

The pharmacokinetic assay of [^{131}I]I-Tyr-D-peptide-PEG$_{11}$-Tz was performed at 1, 3, 5, 10, 15, 30, 60, 120, 360, and 720 min after 1.48 MBq of [^{131}I]I-Tyr-D-peptide-PEG$_{11}$-Tz was injected into male NU/NU mice through the tail vein ($n = 3$). Blood samples (5−10 μL) were collected using capillary tubes at each predetermined time point through the tail vein.

2.15. Click efficiency

We evaluated the of the reaction *in vitro* by mixing [^{131}I]I-Tyr-D-peptide-PEG$_{11}$-Tz and TCO-Per at different molar ratios (1:0, 1:0.2, 1:0.5, and 1:1). After 1 min of reaction, the mixtures were analyzed by sec-HPLC to determine the efficiency.

2.16. Cycloaddition reaction in vivo and in vitro

For cycloaddition reaction *in vivo*, in this experiment, two groups were designed. In the first group of mice, 37 MBq of [^{131}I]I-Tyr-D-peptide-PEG$_{11}$-Tz was administered *via* tail vein injection. One minute later, blood was drawn, and serum was isolated. The serum was then loaded onto a PD-10 desalting column for separation. Elution was carried out using 0.01 mol/L PBS, collecting 0.5 mL fractions in EP tubes. A total of 15 EP tubes containing eluted fractions were collected. The CPM of each EP tubes were subsequently measured to construct the elution profile. In the second group, 200 μg of TCO-Per was injected intravenously, followed 30 min later by 37 MBq of [^{131}I]I-Tyr-D-peptide-PEG$_{11}$-Tz and serum was collected and processed under the same conditions with the first group for constructing the elution profile. For cycloaddition reaction *in vitro,* the click chemistry between TCO-Pertuzumab and [^{131}I]I-Tyr-D-peptide-PEG$_{11}$-Tz was analyzed by SEC-HPLC, and the detailed procedures was provided in the Supporting Information (Supporting Information Fig. S17).

2.17. Single-photon emission computed tomography/computed tomography (SPECT/CT) imaging

Based on the PET imaging results of [^{89}Zr]Zr-DFO-Per, [^{89}Zr]Zr-DFO-Per-F(ab')$_2$ and [^{89}Zr]Zr-DFO-Per-Fab, TCO-Per was selected as the lead molecule. A 48-h interval was chosen between the injection of TCO-Per and [^{131}I]I-Tyr-D-peptide-PEG$_{11}$-Tz. Before intravenous injection of [^{131}I]I-Tyr-D-peptide-PEG$_{11}$-Tz, all the model animals were fed 3% NaI water for 48 h. The mice in Groups I, II, III, and IV received 100 μg of TCO-Per, 200 μg of TCO-Per, 100 μg of TCO-IgG, or 100 μg of TCO-Per (lead molecular), respectively. Groups I, II, and III used the SKOV3 tumor-bearing mouse model ($n = 3$ per group), whereas Group IV used the MGC-803 tumor-bearing mouse model ($n = 3$). All the model mice were intravenously injected with 18.5 MBq of [^{131}I]I-Tyr-D-peptide-PEG$_{11}$-Tz 48 h after intravenous injection of the lead molecule (TCO-Per or TCO-IgG). SPECT/CT imaging was performed 6, 24, 48, 72, and 120 h after injection of [^{131}I]I-Tyr-D-peptide-PEG$_{11}$-Tz for Groups I and II and 24 h for Groups III and IV. The mice were then anaesthetized by 3% isoflurane gas inhalation, and anaesthesia was maintained using 2% isoflurane gas during the SPECT/CT scan. CT was performed with the following parameters for 5 min: algorithm, iterative; tube voltage: 50 kVp; tube current: 0.15 mA; isometric voxel size, 200 μm; and exposure time, 300 ms. SPECT was then performed in the same bed position as the CT scan for 20 min, with the following parameters: algorithm, maximum likelihood expectation maximization; peak, 140 keV; and isometric voxel size, 500 μm. Images were constructed using the maximum likelihood algorithm (50 iterations), and the data were corrected for attenuation.

2.18. Biodistribution of [^{131}I]I-Tyr-D-peptide-PEG$_{11}$-Tz

For the biodistribution assay, a total of four groups were set up, which was similar to SPECT/CT imaging. Group I included 5 time points (6, 24, 48, 72, and 120 h after [^{131}I]I-Tyr-D-peptide-PEG$_{11}$-Tz injection), and Groups II, III and IV included 1 time point (72 h after [^{131}I]I-Tyr-D-peptide-PEG$_{11}$-Tz injection), resulting in a total of 21 SKOV3 tumor models and 3 MGC-803

tumor models included in the biodistribution assay. Tumors, blood, and major tissues/organs (heart, lungs, liver, kidneys, spleen, intestine, stomach, bone and muscles) were harvested and weighed, and the radioactivity count was measured. Tissue radioactivity was expressed as the percentage of injected activity per gram (%IA/g).

2.19. Immunohistochemistry (IHC) and haematoxylin and eosin (H&E) staining

For IHC, after deparaffinization, hydration and antigen retrieval, the tumor sections were incubated in 5% BSA buffer for 1 h. Then, the sections were incubated with anti-HER2 mAb overnight at 4 °C. After being washed in 0.01 mol/L PBS, the sections were stained with an HRP-conjugated goat anti-rabbit antibody for 1 h. Following three 0.01 M PBS washes, 3,3′-diaminobenzidine (DAB) and haematoxylin were used for staining. For H&E staining, after deparaffinization and hydration, H&E staining was performed.

2.20. Pretargeted radionuclide therapy studies and safety evaluation

Pretargeted radionuclide therapy studies were initiated when tumors reached a volume of approximately 200 mm^3. All mice received 100 μg of TCO-Per intravenously 48 h prior to subsequent injections. Mice were randomly assigned to six groups ($n = 5$ per group): 100 μg TCO-Per + 37 MBq [^{131}I]I-Tyr-D-peptide-PEG_{11}-Tz, 100 μg TCO-Per + 7.4 MBq [^{131}I]I-Tyr-D-peptide-PEG_{11}-Tz, normal saline (NS), 100 μg TCO-Per, 37 MBq [^{131}I]I-Tyr-D-peptide-PEG_{11}-Tz and 100 μg Per + 37 MBq [^{131}I]I-Tyr-D-peptide-PEG_{11}-Tz. A single dose was administered at the start of the therapy. Tumor volume and body weight were measured every three days. Mice were euthanized when tumor volume exceeded 1800 mm^3 or upon the occurrence of tumor ulceration. Tumor volume was calculated according to Eq. (1):

$$V = (\text{length} \times \text{width} \times \text{width})/2 \quad (1)$$

Where length is the longest diameter and width is the shortest diameter. Blood cell counts and liver and kidney function were measured to assess the biosafety profile of the treatment. Major organs, including the heart, lungs, liver, spleen, kidneys, and bones, were collected for H&E staining.

2.21. Statistical analysis

The data are presented as the means ± standard deviation (SD) derived from at least three independent experiments. Student's *t* test was performed using GraphPad Prism version 9 (GraphPad Software Inc., La Jolla, CA, USA). Significant differences were considered at $^*P < 0.05$, $^{**}P < 0.01$, and $^{***}P < 0.001$.

3. Results

3.1. HER2 expression levels of SKOV3 and MGC-803 cell lines

The expression levels of HER2 in SKOV3 and MGC-803 cells were quantified using Western blotting, ICC and flow cytometry. SKOV3 cells had a significantly greater relative expression ratio of HER2/β-actin than MGC-803 cells did (1.17 ± 0.17 *vs.* 0.07 ± 0.02, $^{***}P < 0.001$) (Fig. 2A), with the original Western blotting images shown in Supporting Information Fig. S18. The ICC assay revealed that the fluorescence intensity of SKOV3 cells was significantly greater than that of MGC-803 cells (27.94 ± 2.19 *vs.* 2.92 ± 1.48, $^{***}P < 0.001$) (Fig. 2B). HER2 expression levels on the cell membranes of the two cell lines were detected by flow cytometry. The HER2 signal intensity in the SKOV3 cell line (489.17 ± 92.80) was significantly greater than that in the MGC-803 cell line (53.33 ± 1.48) (Fig. 2C). In summary, the SKOV3 cell line has higher expression of HER2 than the MGC-803 cell line.

3.2. Preparation and binding assay of [^{89}Zr]Zr-DFO-Per, [^{89}Zr]Zr-DFO-Per-F(ab')$_2$ and [^{89}Zr]Zr-DFO-Per-Fab

The quality control of Per, Per-F(ab')$_2$ and Per-Fab using SEC-HPLC and gel electrophoresis results were shown in Fig. 3A. The retention time of Per, Per-F(ab')$_2$ and Per-Fab was 8.565, 9.103 and 9.822 min, respectively. The molecular masses of Per, Per-F(ab')$_2$ and Per-Fab were estimated to be approximately 150, 95 and 50 kDa, respectively. The characterization of DFO-Per, DFO-Per-F(ab')$_2$ and DFO-Per-Fab was shown in Supporting Information Fig. S19−S21. Based on LC−MS analysis, the drug-to-antibody ratio (DAR) value of the DFO with DFO-Per, DFO-Per-F(ab')$_2$, and DFO-Per-Fab was 0.44, 0.31, and 0.17, respectively. The [^{89}Zr]Zr-DFO-Per, [^{89}Zr]Zr-DFO-Per-F(ab')$_2$ and [^{89}Zr]Zr-DFO-Per-Fab were successfully synthesized by DFO conjugation, Zr-89 labelling, and purification using PD-10 desalting columns. The radiochemical purities of [^{89}Zr]Zr-DFO-Per, [^{89}Zr]Zr-DFO-Per-F(ab')$_2$ and [^{89}Zr]Zr-DFO-Per-Fab were all approximately 95% (Fig. 3B). The specific activities of [^{89}Zr]Zr-DFO-Per, [^{89}Zr]Zr-DFO-Per-F(ab')$_2$ and [^{89}Zr]Zr-DFO-Per-Fab were (2.05 ± 0.14) × 10^7 MBq/mmol, (1.34 ± 0.26) × 10^7 MBq/mmol, (1.49 ± 0.21) × 10^7 MBq/mmol, respectively. For the binding assay, the equilibrium binding constant (K_d) of [^{89}Zr]Zr-DFO-Per, [^{89}Zr]Zr-DFO-Per-F(ab')$_2$ and [^{89}Zr]Zr-DFO-Per-Fab for HER2 was 16.31 ± 1.20, 16.59 ± 1.82 and 27.07 ± 1.38 nmol/L, respectively, with corresponding B_{max} was 675 ± 91 CPS, 597 ± 89 CPS and 615 ± 24 CPS (Supporting Information Fig. S22).

3.3. Determination of the optimal lead molecule and metabolic timing by micro-PET/CT of [^{89}Zr]Zr-DFO-Per, [^{89}Zr]Zr-DFO-Per-F(ab')$_2$ and [^{89}Zr]Zr-DFO-Per-Fab

The [^{89}Zr]Zr-DFO-Per, [^{89}Zr]Zr-DFO-Per-F(ab')$_2$ and [^{89}Zr]Zr-DFO-Per-Fab micro-PET/CT imaging results were shown in Fig. 3C−E. We aimed to find the optimal lead molecule using micro-PET/CT and determine the optimal injection interval between the lead molecule and the radiolabelled small-molecule Tz. As shown in Fig. 3C−E, the [^{89}Zr]Zr-DFO-Per group presented the highest target-to-background ratio, indicating that Per is the optimal lead molecule for further investigation. [^{89}Zr]Zr-DFO-Per was metabolized primarily by the liver. After [^{89}Zr]Zr-DFO-Per postinjection for 48 h, almost all of the radioactivity was concentrated in the SKOV3 tumor region. To further quantify the distribution of [^{89}Zr]Zr-DFO-Per *in vitro*, biodistribution studies were conducted at 6, 24, 48, 72, and 120 h post-injection in SKOV3 tumor-bearing mice ($n = 3$) (Supporting Information Fig. S23). Consistent with the micro-PET/CT imaging results, the %IA/g (percentage of injected activity per gram) value in the blood pool remained elevated up to 48 h. The tracer was predominantly metabolized by the liver, with uptake values of

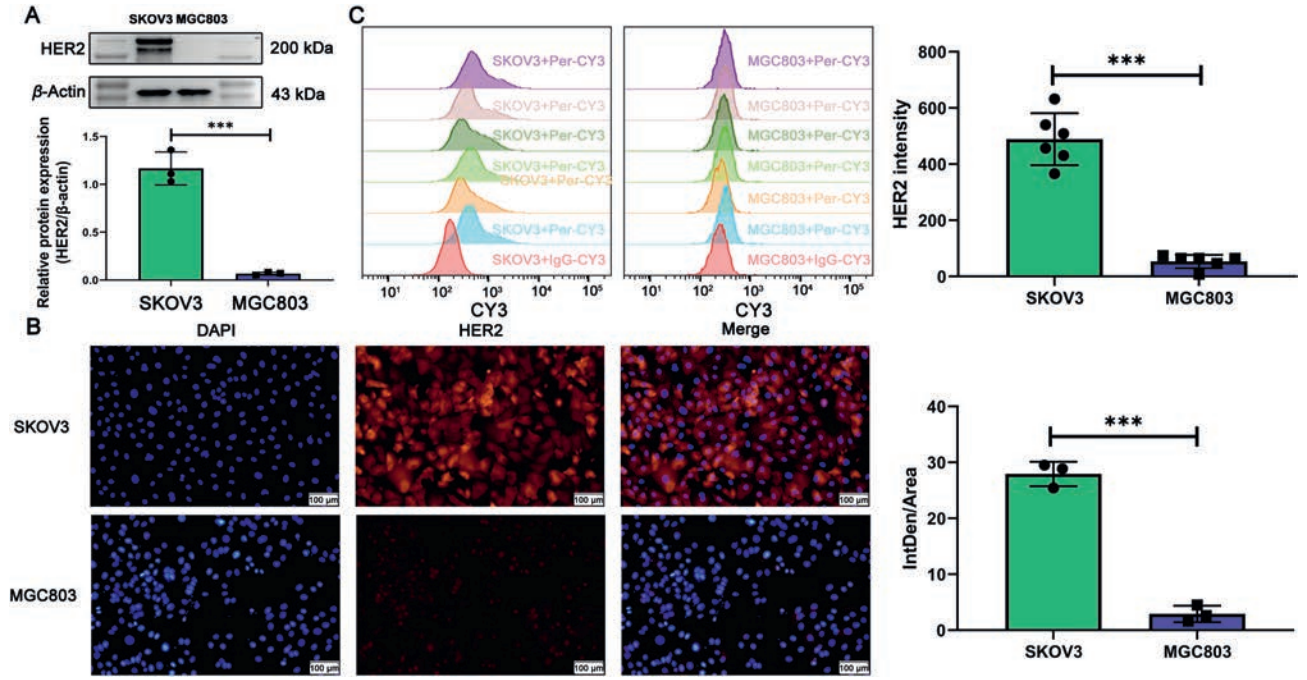

Figure 2 Comparison of HER2 protein expression levels in the SKOV3 and MGC-803 cell lines. The HER2 protein expression level was determined by Western blotting (A), ICC Scale bar: 100 μm (B) and flow cytometry (C).

13.78 ± 3.34, 7.54 ± 1.44, and 4.69 ± 0.76 %IA/g at 6, 24, and 48 h, respectively. In addition, a limited but persistent increase in bone uptake was observed, with %IA/g values of 3.02 ± 0.06, 3.19 ± 0.83, and 4.03 ± 0.48 at 6, 24, and 48 h, respectively. Because [^{89}Zr]Zr-DFO-Per accumulated in the tumor region after 48 h, we used this time interval as the injection time difference between the lead molecule (TCO-Per) and the radiolabelled small molecule ([^{131}I]I-Tyr-D-peptide-PEG$_{11}$-Tz). In addition, we performed micro-PET/CT imaging on blocking group and HER2-negative expressing group to demonstrate the *in vivo* specificity of [^{89}Zr]Zr-DFO-Per (Supporting Information Fig. S24).

3.4. Synthesis, quality control, stability, octanol-water partition coefficient and pharmacokinetic assays of [^{131}I]I-Tyr-D-peptide-PEG$_{11}$-Tz

The detailed synthesis results of the precursor Tyr-D-peptide-PEG$_{11}$-Tz were shown in Supporting Information The D-peptide moiety consists of six amino acids with the sequence Gly-Arg-Glu-Arg-Glu-Lys, which were introduced to enhance the hydrophilicity of the probe. The structural formula of [^{131}I]I-Tyr-D-peptide-PEG$_{11}$-Tz was shown in Fig. 4A. The radiochemical yield of [^{131}I]I-Tyr-D-peptide-PEG$_{11}$-Tz was greater than 95%, and after semi-HPLC purification, the radiochemical purity of [^{131}I]I-Tyr-D-peptide-PEG$_{11}$-Tz was approximately 99% (Fig. 4B). Furthermore, MS analysis was performed to confirm the molecular weight of [^{nat}I]I-Tyr-D-peptide-PEG$_{11}$-Tz, thereby verifying that the synthesized product corresponded to the intended target compound (Supporting Information Fig. S25). The apparent specific activity of [^{131}I]I-Tyr-D-peptide-PEG$_{11}$-Tz was (7.42 ± 0.33) × 10^4 MBq/μmol. The excellent *in vitro* stability of [^{131}I]I-Tyr-D-peptide-PEG$_{11}$-Tz, which maintains a radiochemical purity greater than 94% after 120 h of incubation in either 0.01 mol/L PBS or 10% FBS, was crucial for its ability to remain in the tumor for extended periods, enabling effective tumor killing (Fig. 4C). In addition, *in vivo* stability was assessed. Owing to the relatively rapid blood clearance, the tracer could not be detected in circulation beyond 24 h. At 24 h post-injection, its radiochemical purity remained above 98% (Fig. 4D). The strong hydrophilicity of [^{131}I]I-Tyr-D-peptide-PEG$_{11}$-Tz, reflected by its log*D* value of -2.158 ± 0.116, allows rapid renal clearance, thereby minimizing the cumulative radiation dose. The pharmacokinetic assay revealed that the distribution half-life of [^{131}I]I-Tyr-D-peptide-PEG$_{11}$-Tz was 5.29 ± 2.25 min and that the elimination half-life was 48.96 ± 5.92 min (Supporting Information Fig. S26).

3.5. Click reaction confirmation in vivo, click efficiency in vitro, specificity in vitro and binding assays of the radionuclide targeting delivery system

The characterization of TCO-Per was shown in Fig. S1B. Based on LC−MS analysis, an average of 1.71 mol TCO-NHS ester molecules were conjugated per mole of Per. *In vitro*, upon mixing TCO-Per and [^{131}I]I-Tyr-D-peptide-PEG$_{11}$-Tz, a significant click chemistry reaction occurred instantaneously, as shown in Supporting Information Fig. S17. To confirm that this pre-targeting combination achieves *In vivo* binding, we carried out two experimental setups. First, following tail vein injection of [^{131}I]I-Tyr-D-peptide-PEG$_{11}$-Tz, mouse serum was prepared and separated using a PD-10 desalting column. Significant radioactivity was observed in tubes 8-10 ([^{131}I]I-Tyr-D-peptide-PEG$_{11}$-Tz) (Fig. 4E). Second, when TCO-Per was administered prior to tail vein injection of [^{131}I]I-Tyr-D-peptide-PEG$_{11}$-Tz, the PD-10 desalting column separation of mouse serum revealed two peaks of radioactivity. The first peak corresponded to [^{131}I]I-Tyr-D-peptide-PEG$_{11}$-Tz-TCO-Per, while the second peak represented [^{131}I]I-Tyr-D-peptide-PEG$_{11}$-Tz, demonstrating that the *in vivo* click chemistry reaction of this pre-targeting combination was

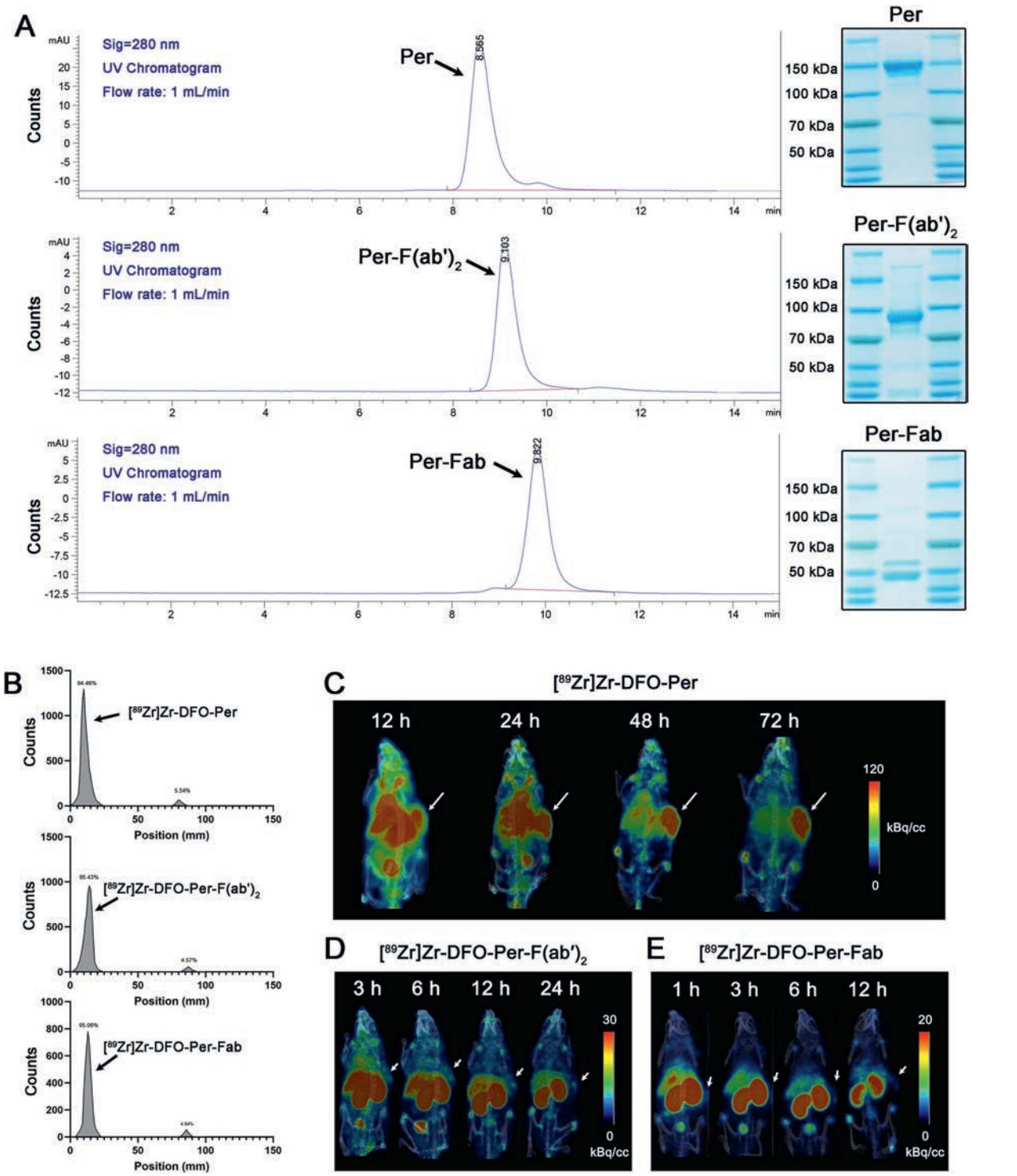

Figure 3 Preparation, quality control, and micro-PET/CT results of [^{89}Zr]Zr-DFO-Per, [^{89}Zr]Zr-DFO-Per-F(ab')$_2$ and [^{89}Zr]Zr-DFO-Per-Fab. (A) SEC-HPLC and SDS-PAGE results for Per, Per-F(ab')$_2$, and Per-Fab. (B) The iTLC results of [^{89}Zr]Zr-DFO-Per, [^{89}Zr]Zr-DFO-Per-F(ab')$_2$ and [^{89}Zr]Zr-DFO-Per-Fab. (C) Representative micro-PET/CT MIP images of SKOV3 tumor-bearing model mice injected with [^{89}Zr]Zr-DFO-Per at 12, 24, 48 and 72 h. (D) Representative micro-PET/CT MIP images of SKOV3 tumor-bearing model mice injected with [^{89}Zr]Zr-DFO-Per-F(ab')$_2$ at 3, 6, 12 and 24 h. (E) Representative micro-PET/CT MIP images of SKOV3 tumor-bearing model mice injected with [^{89}Zr]Zr-DFO-Per-Fab at 1, 3, 6, and 12 h. White arrows in (C−E) indicated the tumor locations.

successfully completed (Fig. 4F). The click efficiency *in vitro* between [^{131}I]I-Tyr-D-peptide-PEG$_{11}$-Tz and TCO-Per was assessed in four molar ratios, showing a progressive increase with the rising proportion of [^{131}I]I-Tyr-D-peptide-PEG$_{11}$-Tz and reaching a maximum of 83.66 ± 1.57% at a 1:1 ratio (Fig. 4G). For the binding assay, the equilibrium binding constant (K_d) of

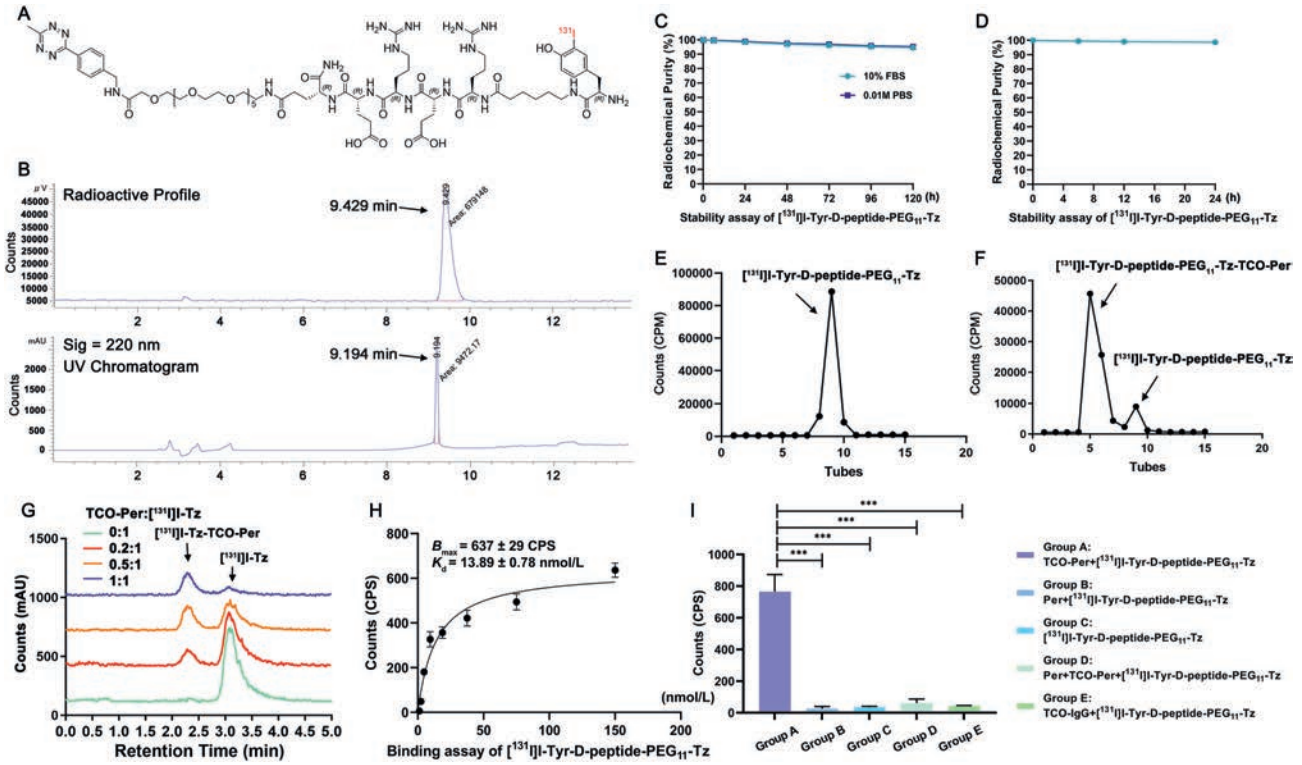

Figure 4 Physicochemical and biological characteristics of the radionuclide targeting delivery system. (A) The structural formula of [^{131}I]I-Tyr-D-peptide-PEG$_{11}$-Tz. (B) The radio-HPLC results of [^{131}I]I-Tyr-D-peptide-PEG$_{11}$-Tz. (C) Stability assay *in vitro* of [^{131}I]I-Tyr-D-peptide-PEG$_{11}$-Tz. (D) Stability assay *in vivo* of [^{131}I]I-Tyr-D-peptide-PEG$_{11}$-Tz. (E, F) Bioorthogonal click *in vivo* experiment of the TCO-Per/[^{131}I]I-Tyr-D-peptide-PEG$_{11}$-Tz system. (G) Assessment of [^{131}I]I-Tyr-D-peptide-PEG$_{11}$-Tz-TCO-Per click efficiency *in vitro*. (H) Binding assay of [^{131}I]I-Tyr-D-peptide-PEG$_{11}$-Tz-TCO-Per. (I) Specificity of [^{131}I]I-Tyr-D-peptide-PEG$_{11}$-Tz.

[^{131}I]I-Tyr-D-peptide-PEG$_{11}$-Tz-TCO-Per for HER2 was 13.89 ± 0.78 nmol/L, and the B_{max} was 637 ± 29 CPS (Fig. 4H). This affinity was comparable to that of the ^{89}Zr-labelled antibodies, indicating that the pretargeting system preserved the high binding affinity of the parental antibody and that the bioorthogonal click conjugation did not impair antigen recognition. For the *in vitro* specificity assay shown in Fig. 4I, we demonstrated, through five distinct experimental groups, the necessity of both [^{131}I]I-Tyr-D-peptide-PEG$_{11}$-Tz and TCO-Per in the radionuclide targeting delivery system as well as their excellent *in vitro* specificity.

3.6. SPECT/CT imaging of the radionuclide targeting delivery system

Fig. 5 presented the representative micro-SPECT/CT maximum intensity projection (MIP) imaging results of the tumor-bearing mouse model. The workflow of SPECT/CT imaging was shown in Fig. 5A. All animal models in Group I and Group II received an intravenous injection of TCO-Per *via* the tail vein 48 h before the second intravenous injection of 18.5 MBq [^{131}I]I-Tyr-D-peptide-PEG$_{11}$-Tz (0.24−0.26 nmol). Micro-SPECT/CT imaging was performed at 6, 24, 48, 72, and 120 h after injecting [^{131}I]I-Tyr-D-peptide-PEG$_{11}$-Tz. The only difference between the two groups was the dose of TCO-Per (100 or 200 μg). Micro-SPECT/CT MIP indicated that the injection of 100 or 200 μg of TCO-Per did not significantly affect the distribution of [^{131}I]I-Tyr-D-peptide-PEG$_{11}$-Tz in the animal models (Fig. 5B and C). Additionally, [^{131}I]I-Tyr-D-peptide-PEG$_{11}$-Tz was eliminated primarily through the kidneys. Within 24 h of [^{131}I]I-Tyr-D-peptide-PEG$_{11}$-Tz injection, the renal radioactivity distribution surpassed that of all other organs and tissues, including tumors. The tumor site presented the highest radioactivity distribution at 48 h postinjection of [^{131}I]I-Tyr-D-peptide-PEG$_{11}$-Tz. Importantly, the radioactivity distribution in other tissues or organs, excluding the tumor, was extremely low. This significantly reduces the cumulative radiation dose to nontarget organs and minimizes the side effects associated with radiation damage. This radionuclide targeting delivery system demonstrated significant advantages over the direct labelling approach, which uses Per as the targeting molecule. In addition, [^{131}I]I-Tyr-D-peptide-PEG$_{11}$-Tz showed excellent *In vivo* specificity, with significantly reduced uptake at tumor sites in both the TCO-IgG (Group III) and the MGC-803 groups (Group IV), consistent with the *in vitro* specificity results (Fig. 5D and E).

3.7. Biodistribution of the radionuclide targeting delivery system and histological analysis

To further quantify the radioactivity distribution in various organs and tissues of the tumor-bearing mice, we conducted an *in vitro* biodistribution study. The overall workflow is shown in Fig. 6A. The animal grouping for biodistribution studies was the same as that used for micro-SPECT/CT imaging of the radionuclide targeting delivery system, the tracer dose was approximately 1.1−1.9 MBq (0.015−0.025 nmol). The biodistribution results of Group I are presented in Fig. 6B, which revealed a rapid decrease in

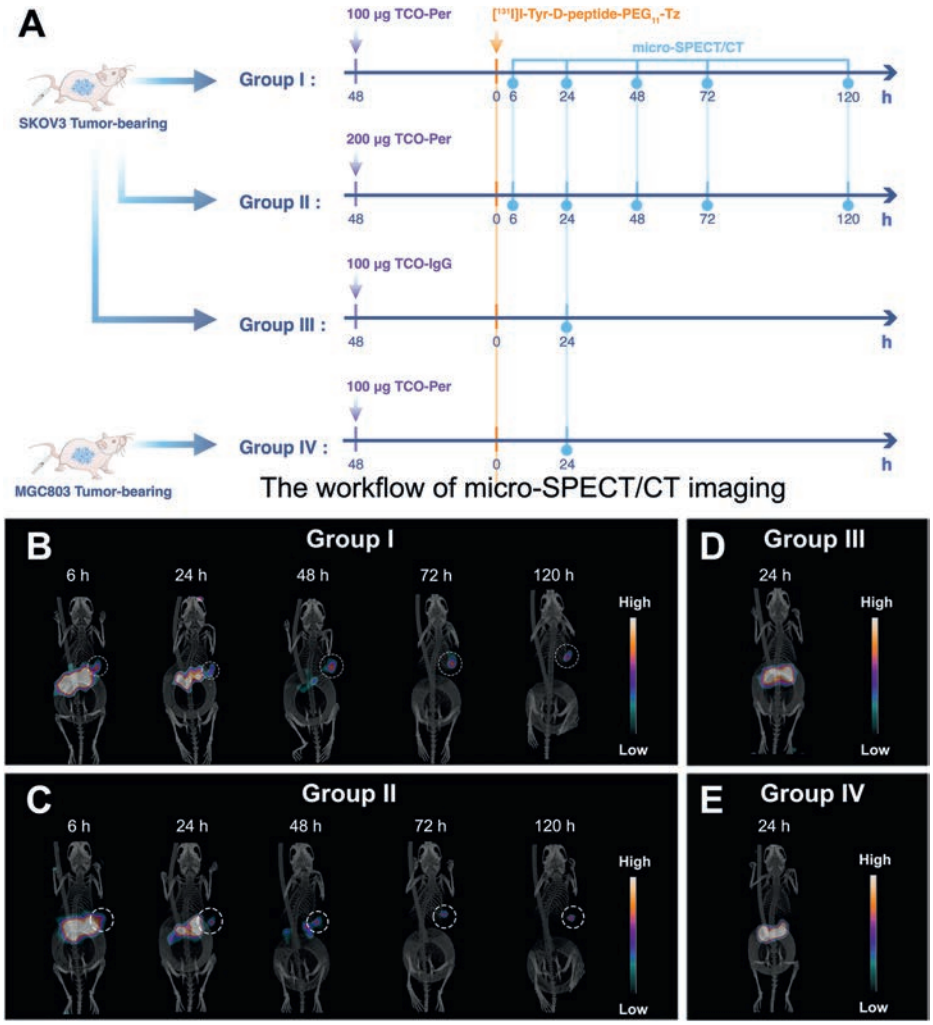

Figure 5 Micro-SPECT/CT imaging of the radionuclide targeting delivery system. (A) Overall workflow for micro-SPECT/CT imaging of the radionuclide targeting delivery system. (B) Representative micro-SPECT/CT MIP images of the radionuclide targeting delivery system in a SKOV3 tumor-bearing mouse model (100 μg TCO-Per). (C) Representative micro-SPECT/CT MIP images of the radionuclide targeting delivery system in a SKOV3 tumor-bearing mouse model (200 μg TCO-Per). (D, E) Representative micro-SPECT/CT MIP images of the radionuclide targeting delivery system with an isotype control group (TCO-IgG) (D) and a negative control group (MGC803 tumor-bearing mouse model) (E).

radioactivity distribution within the kidneys, confirming that [^{131}I]I-Tyr-D-peptide-PEG$_{11}$-Tz was eliminated through renal metabolism. At 48 h postinjection of the probe [^{131}I]I-Tyr-D-peptide-PEG$_{11}$-Tz, the tumor became the tissue with the highest radioactivity distribution. Moreover, until 120 h, although the radioactivity distribution in the tumor decreased slowly, it remained the tissue with the highest radioactivity. The tumor/muscle (T/M) ratios at 6, 24, 48, 72 and 120 h postinjection of [^{131}I]I-Tyr-D-peptide-PEG$_{11}$-Tz were 6.26 ± 1.95, 10.02 ± 1.30, 11.06 ± 1.43, 11.73 ± 1.15 and 11.92 ± 0.66, respectively. This consistently high target-to-nontarget ratio ensured stable radioactivity exposure to the tumor site, potentially leading to ideal therapeutic outcomes. Additionally, to verify the specificity of TCO-Per/[^{131}I]I-Tyr-D-peptide-PEG$_{11}$-Tz, a comparative study was conducted among the four groups (Fig. 6C). The results indicated that tumor uptake of the Tz-radioligand in Group III (0.34 ± 0.14 %IA/g) and Group IV (0.48 ± 0.25 %IA/g) was significantly lower than that in Group I (2.17 ± 0.36 %IA/g) and Group II (2.27 ± 0.52 %IA/g). These findings confirmed that the TCO-Per/[^{131}I]I-Tyr-D-peptide-PEG$_{11}$-Tz radionuclide targeting delivery system exhibited excellent specificity, a finding that was consistent with the *in vitro* specificity and micro-SPECT/CT imaging results. Regarding safety, analysed by the distribution data of Group I, [^{131}I]I-Tyr-D-peptide-PEG$_{11}$-Tz consistently showed a low distribution in the blood and liver (Fig. 6D). The tumor/blood (T/B) ratios at 6, 24, 48, 72 and 120 h postinjection of [^{131}I]I-Tyr-D-peptide-PEG$_{11}$-Tz were 5.08 ± 1.26, 8.58 ± 2.09, 12.95 ± 1.08, 15.54 ± 2.13 and 15.41 ± 1.61, respectively. The tumor/liver (T/L) ratios at 6, 24, 48, 72 and 120 h postinjection of [^{131}I]I-Tyr-D-peptide-PEG$_{11}$-Tz were 3.85 ± 0.77, 5.81 ± 0.84, 6.37 ± 0.44, 6.99 ± 0.94 and 6.35 ± 0.28, respectively; this may indicate a reduced probability of adverse reactions such as thrombocytopenia and hepatotoxicity. Fig. 6E presented the biodistribution results of [^{131}I]I-Tyr-D-peptide-PEG$_{11}$-Tz in SKOV3 tumor-bearing mice models without prior injection of TCO-Per. The data demonstrated that [^{131}I]I-Tyr-D-peptide-PEG$_{11}$-Tz alone did not exhibit significant tumor targeting without the priming effect of TCO-Per. Moreover, Consistent with the log*D* value, the hydrophilic nature of [^{131}I]I-Tyr-D-peptide-PEG$_{11}$-Tz led to its primary elimination through the kidneys. The biodistribution of

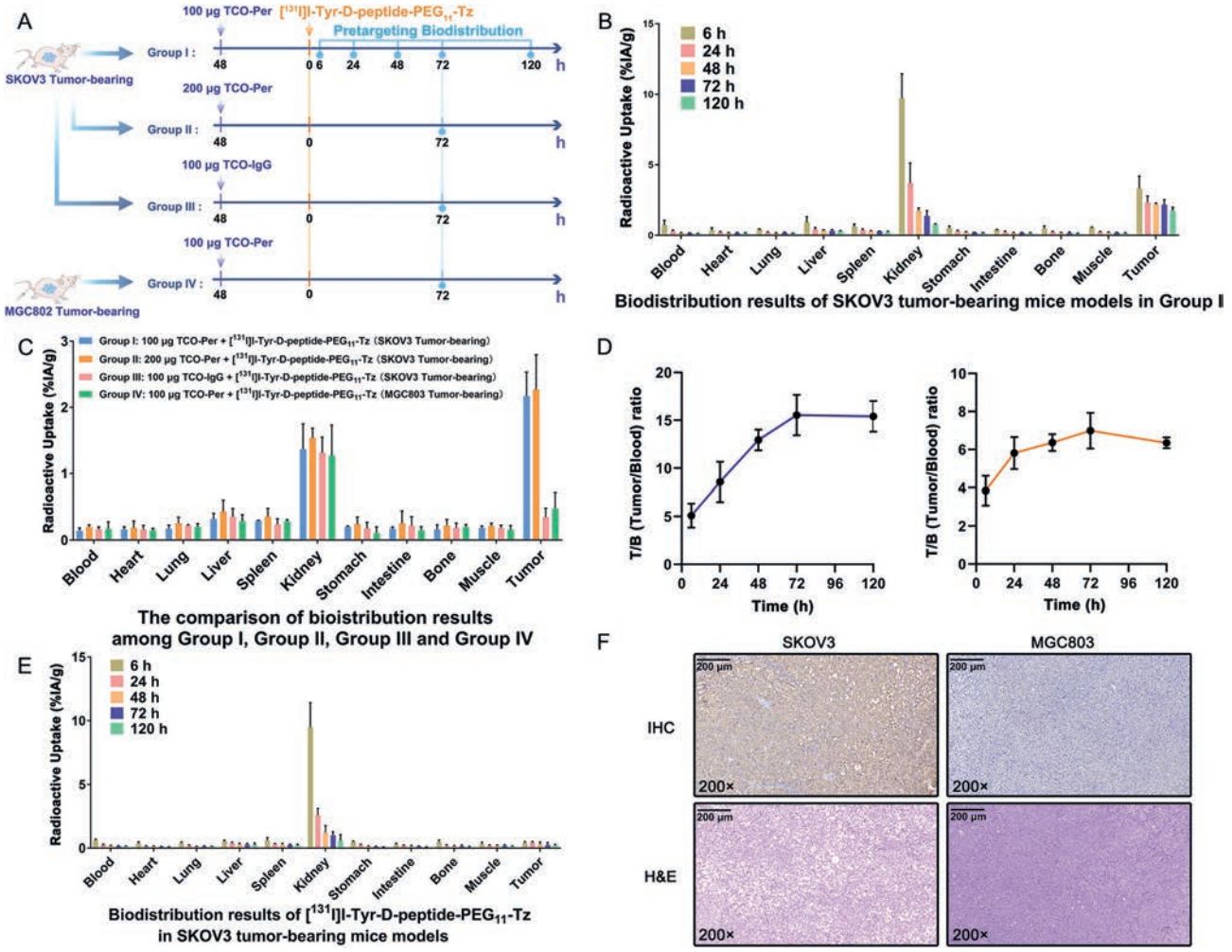

Figure 6 Comparative biodistribution of [^{131}I]I-Tyr-D-peptide-PEG$_{11}$-Tz in SKOV3 tumor-bearing model mice pre-injection with 100 μg of TCO-Per, 200 μg of TCO-Per, 100 μg of TCO-IgG or the negative control (MGC-803 tumor-bearing mouse model). (A) Grouping and workflow of biodistribution assays. (B) Biodistribution results of Group I at 6, 24, 48 72 and 120 h timepoints. (C) Comparative biodistribution assays among four groups at 72 h postinjection of [^{131}I]I-Tyr-D-peptide-PEG$_{11}$-Tz. (D) The T/B and T/L ratio of Group I. (E) Biodistribution results of [^{131}I]I-Tyr-D-peptide-PEG$_{11}$-Tz in SKOV3 tumor-bearing mice models without prior injection of TCO-Per. (F) H&E (200 ×) and IHC (200 ×) staining of SKOV3 and MGC803 tumor sections.

[^{131}I]I-Tyr-D-peptide-PEG$_{11}$-Tz in other tissues/organs remained low from 6 to 120 h, with a gradual decrease over time. In addition, the biodistribution of Group I was compared with that of [^{89}Zr]Zr-DFO-Per (Supporting Information Fig. S27). [^{89}Zr]Zr-DFO-Per exhibited markedly higher uptake than [^{131}I]I-Tyr-D-peptide-PEG$_{11}$-Tz in most major organs, including the blood, liver, spleen, lungs, and bones. The only exception was the kidneys, where [^{131}I]I-Tyr-D-peptide-PEG$_{11}$-Tz showed higher accumulation, consistent with its renal excretion pathway. In the tumor, uptake of [^{89}Zr]Zr-DFO-Per was also higher; however, its tumor-to-blood and tumor-to-liver ratios were significantly lower than those of [^{131}I]I-Tyr-D-peptide-PEG$_{11}$-Tz, indicating that the latter provided superior imaging contrast. Fig. 6F shows representative microscopy images of SKOV3 and MGC-803 tumor sections (5 μm thick) subjected to H&E staining and IHC staining for HER2. The positive rate for HER2 staining in SKOV3 tumor tissue was significantly greater than that in MGC-803 tumor tissue, a finding that was consistent with the results of western blotting, ICC and flow cytometry.

3.8. *Therapy studies*

In the therapy study, tumor volumes were continuously monitored for 27 days. By day 27, tumors in both the normal saline (NS) group and the group treated with 37 MBq [^{131}I]I-Tyr-D-peptide-PEG$_{11}$-Tz alone exceeded 1800 mm^3, with mean tumor volumes of 1990.80 ± 208.11 and 1998.50 ± 229.69 mm^3, respectively. In contrast, tumor growth was suppressed to varying extents in the remaining four treatment groups (Fig. 7A). Specifically, mice treated with 100 μg TCO-Per (1517.80 ± 160.00 mm^3) or 100 μg Per + 37 MBq [^{131}I]I-Tyr-D-peptide-PEG$_{11}$-Tz (1454.70 ± 136.88 mm^3) exhibited only modest tumor growth inhibition, likely due to the absence of an *in vivo* bioorthogonal click reaction. The group receiving 100 μg TCO-Per +7.4 MBq [^{131}I]I-Tyr-D-peptide-PEG$_{11}$-Tz (1278.20 ± 134.88 mm^3) showed limited therapeutic efficacy, which may be attributed to the lower administered radioactivity. Notably, tumor growth was most significantly suppressed in mice treated with 100 μg TCO-Per +37 MBq

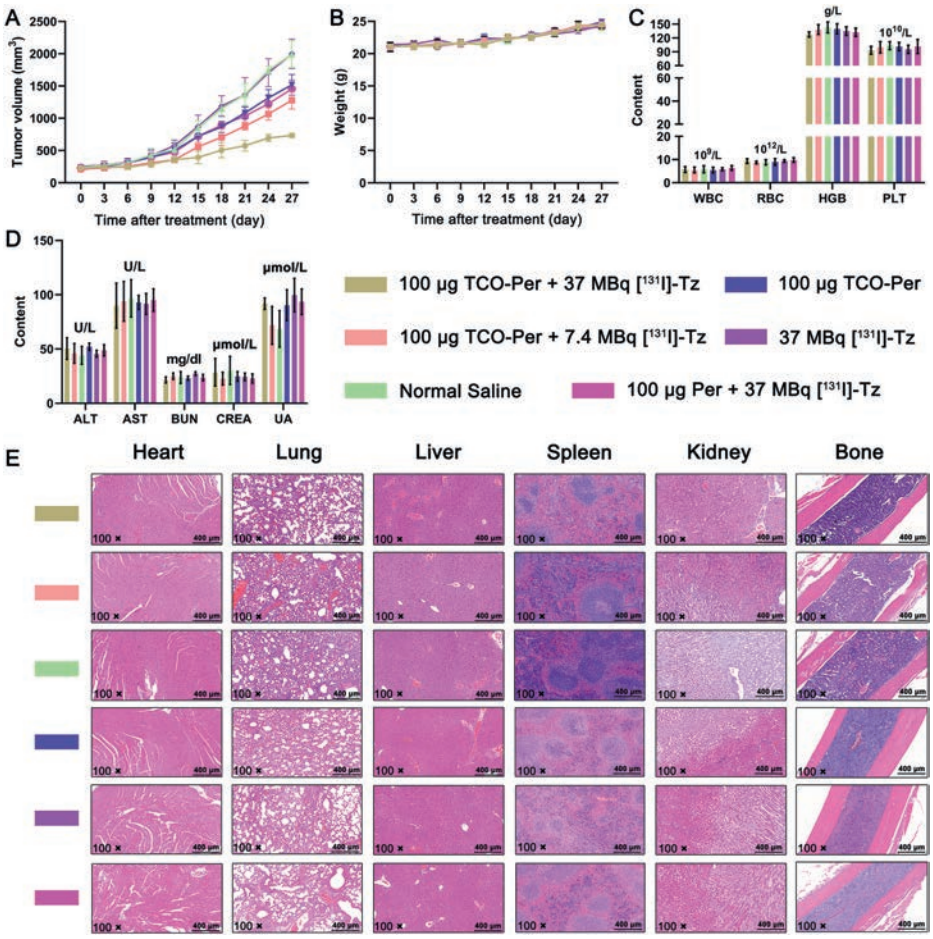

Figure 7 Efficacy of radioligand therapy of SKOV3 tumor-bearing mice models injected with a single dose of [^{131}I]I-Tyr-D-peptide-PEG$_{11}$-Tz. (A) The tumor volume monitoring of each group. (B) Bodyweight change of tumor-bearing mice during the therapy study. (C) Blood count tests of each group at the end of the therapy. (D) Liver and kidney function tests for mice of each group at the end of the therapy. (E) H&E staining of organs in each group (100 ×). All treatment groups, except for the 37 MBq [^{131}I]I-Tyr-D-peptide-PEG$_{11}$-Tz alone group, exhibited significant tumor growth inhibition compared with the saline control ($n = 5$ per group, one-way ANOVA followed by Dunnett's multiple comparisons test, $P < 0.001$) (A). No statistically significant differences were observed among groups in hematological parameters (C) or liver and kidney function indices (D) ($n = 5$ per group, one-way ANOVA followed by Dunnett's multiple comparisons test, $P > 0.05$). WBC: white blood cell; RBC: red blood cell; HGB: hemoglobin; PLT: platelet; ALT: alanine transaminase; AST: aspartate aminotransferase; BUN: blood urea nitrogen; CREA: creatinine; and UA: uric acid.

[^{131}I]I-Tyr-D-peptide-PEG$_{11}$-Tz, with a mean tumor volume of 732.90 ± 32.01 mm^3, demonstrating the pronounced therapeutic benefit of the pretargeted click-based strategy. No deaths occurred during the 27-day monitoring period, and body weights showed no significant differences among groups (Fig. 7B). Complete blood counts and liver and kidney function tests in all six groups indicated that even in the highest dose group, no significant bone marrow suppression or liver/kidney damage was detected (Fig. 7C and D). H&E staining of major organs further confirmed the biosafety of this therapeutic strategy (Fig. 7E).

4. Discussion

For patients with advanced solid tumors, systemic chemotherapy is usually the foundation of treatment and is often combined with local radiotherapy or systemic immunotherapy to combat the tumor. However, drug resistance after multiple cycles of anti-tumor treatment is inevitable. Therefore, new therapeutic strategies are needed to address the progression of advanced solid tumors. Radionuclide therapy holds immense potential for treating advanced solid tumors. On March 23, 2022, Pluvicto[14] ([^{177}Lu]Lu-PSMA-617) received Food and Drug Administration (FDA) approval for the treatment of adult patients with prostate-specific membrane antigen (PSMA)-positive metastatic castration-resistant prostate cancer (mCRPC) who received androgen receptor (AR) inhibitors and taxane-based chemotherapy. Compared with standard of care (SOC), Pluvicto combined with SOC effectively prolonged patients' median progression-free survival (mFPS) (8.7 months *vs.* 3.4 months) and reduced the risk of disease progression or death by 60% (HR 0.40). Since its approval, Pluvicto has been in high demand worldwide. Currently, only a handful of radiopharmaceuticals for solid tumors have been approved for clinical use. There is a need to develop new targets and novel radiolabelled probes to meet clinical needs.

HER2 is overexpressed in a variety of solid tumors, including ovarian cancer and breast cancer, making it a suitable target for

theranostics in nuclear medicine[15,16]. In recent years, the indications for HER2-targeted therapies have expanded beyond breast cancer and ovarian cancer to encompass a broader range of solid tumors[3]. Currently, there are multiple PET molecular probes targeting HER2, guided by IgG monoclonal antibodies, undergoing clinical trials, including [^{64}Cu]Cu-DOTA-trastuzumab[6,7], [^{89}Zr]Zr-trastuzumab[8,9]. However, HER2-targeted radioimmunotherapy guided by IgG monoclonal antibodies has largely remained in the preclinical stage. While radiolabelled monoclonal antibodies retain the advantages of high affinity and specificity, they also retain the drawback of long circulation times *in vivo*. An IgG antibody has an approximate molecular weight of 150 kDa, and its serum half-life ($T_{1/2}$) is $>$ 2 day (the serum half-life of the IgG subclasses IgG1, IgG2, and IgG4 is $\sim$23 days *versus* 2−6 days for IgG3 and other Ig classes)[17]. The prolonged circulation of radiolabelled monoclonal antibodies *In vivo* may cause damage to blood cells and metabolic organs.

While targeted radionuclide therapy, including high-linear energy transfer α-particle-based approaches such as [^{225}Ac]Ac-labelled antibodies, has demonstrated promising therapeutic efficacy in preclinical solid tumor models, these studies also highlight that therapeutic outcomes are critically dependent on accurate tumor targeting and intratumoral radionuclide distribution[18]. Moreover, systemic toxicity and off-target radiation exposure remain major challenges that limit dose escalation when radionuclides are directly conjugated to long-circulating antibodies.

To address this drawback, a pretargeting strategy-based radionuclide delivery system was developed. Currently, there are four main pretargeting systems: the streptavidin-biotin system, the bispecific antibody (bsAb) system, the complementary oligonucleotide hybridization system, and the bioorthogonal IEDDA click reaction[19-22]. In addition to the TCO/Tz-based HER2-targeting radionuclide delivery system reported in this study, James C Knight et al. reported a novel radionuclide delivery system: the dehalogenase enzyme HaloTag and a chloroalkane HaloTag ligand. It proceeds with a second-order rate constant of 2.7×10^6 M^{-1} s^{-1}, which is comparable to that of the biotin/(strept)avidin reaction, and importantly, the HaloTag enzyme does not suffer interference from competing endogenous substrates, rendering it fully available to the HTL secondary agent[23]. However, HaloTag has a large molecular weight, approximately 33 kDa, which significantly increases the molecular weight of the lead molecule and thus slows its metabolism. Maryam Oroujeni et al. introduced another peptide nucleic acid (PNA)-mediated HER2-targeting radionuclide delivery system[24]. They used Affibody-PNA as the lead molecule and employed another complementary PNA probe to achieve the pretargeting strategy. Among these systems, IEDDA click chemistry offers advantages such as high stability y, mild reaction conditions, and rapid reaction speed[25]. Bioorthogonal pretargeting strategies have recently demonstrated great potential for multimodal tumor imaging by enabling highly specific *in situ* labelling with reduced background interference, highlighting the versatility of pretargeted approaches in oncological applications[26]. Therefore, we selected the IDEEA click chemistry (TCO/Tz) strategy to achieve radionuclide targeting delivery system. The radionuclide delivery system involves the introduction of a large-molecule lead molecule (TCO-Per in this study) into mouse models for metabolic clearance. After the lead molecule is eliminated from nontarget organs, a small-molecule radiolabelled Tz ([^{131}I]I-Tyr-D-peptide-PEG$_{11}$-Tz in this study) is introduced. This strategy combines the advantages of high specificity and affinity of the lead molecule (TCO-Per) with the rapid metabolic clearance rate of the small Tz ([^{131}I]I-Tyr-D-peptide-PEG$_{11}$-Tz). Besides IDEEA reaction, the streptavidin-biotin system, the bsAb system and the complementary oligonucleotide hybridization system could be used for radionuclide delivery[19-22]. The IEDDA reaction was selected based on its favourable characteristics, including rapid reaction, mild reaction conditions, and the formation of a stable linkage.

In this study, we prepared three antibody-based candidates, Per, Per-F(ab')$_2$, and Per-Fab, and aimed to identify the optimal lead molecules using micro-PET/CT imaging. The antibody fragments were designed by removing the nonspecific Fc region, with the expectation of retaining antigen specificity while reducing molecular weight, thereby accelerating blood clearance and minimizing radiation accumulation in non-target organs. After labelling with ^{89}Zr for PET imaging and biodistribution, [^{89}Zr]Zr-DFO-Per demonstrated the highest tumor-to-background ratio, and was therefore selected as the lead molecule for radionuclide delivery system. Although the [^{89}Zr]Zr-DFO-Per-F(ab')$_2$ and [^{89}Zr]Zr-DFO-Per-Fab retained comparable *in vitro* affinities to the [^{89}Zr]Zr-DFO-Per, their *in vivo* tumor uptake was markedly reduced. This discrepancy is likely attributable to their smaller molecular sizes, which result in rapid renal clearance and the absence of FcRn-mediated recycling, thereby limiting blood circulation time and tumor accumulation[27,28]. Simultaneously, based on the micro-PET/CT imaging results, we determined the optimal time interval (48 h) between the lead molecule (TCO-Per) and the radiolabelled Tz ([^{131}I]I-Tyr-D-peptide-PEG$_{11}$-Tz).

The radiolabelled precursor (Tyr-D-peptide-PEG$_{11}$-Tz) was designed based on our previous research. Starting from the tetrazine moiety, a methyl-substituted tetrazine was employed to enhance stability. Methyl substitution on the tetrazine ring is known to reduce IEDDA reaction kinetics but significantly enhance *in vivo* stability compared with unsubstituted tetrazines, as reported previously[29]. This trade-off between reactivity and stability guided our probe design. In addition, a methyl-substituted tetrazine was employed in this study to further enhance stability. Since Tz is highly lipophilic, unmodified radiolabelled Tz typically shows substantial hepatic accumulation[30,31]. To improve hydrophilicity, Lin Qiu et al.[32] introduced PEG$_{11}$ and synthesized [^{99m}Tc]Tc-HYNIC-PEG$_{11}$-Tz, which displayed extremely low uptake in the liver and kidneys but high intestinal radioactivity, suggesting biliary excretion. To further redirect clearance from hepatobiliary to renal excretion, hydrophilicity was enhanced by incorporating a polypeptide (Gly-Arg-Glu-Arg-Glu-Lys), resulting in [^{99m}Tc]Tc-HYNIC-Polypeptide-PEG$_{11}$-Tz and [^{68}Ga]Ga-NOTA-polypeptide-PEG$_{11}$-Tz, both of which were predominantly cleared *via* the kidneys[33,34]. However, the stability of [^{99m}Tc]Tc-HYNIC-Polypeptide-PEG$_{11}$-Tz and [^{68}Ga]Ga-NOTA-polypeptide-PEG$_{11}$-Tz exhibited limited stability, retaining only $\sim$80% radiochemical purity after 3 h of incubation *in vitro*. We attributed this instability to the polypeptide chain. Therefore, in this study, the entire polypeptide was replaced with D-amino acids to markedly improve stability, while preserving hydrophilicity. Peptide radioiodination is typically achieved either by electrophilic substitution on tyrosine or *via* prosthetic groups (*e.g.*, the Bolton-Hunter method). While the latter yields a benzoate C-I bond with higher metabolic stability and broad amine conjugation, it can react with any amino group and is thus less suitable for our probe design, being more appropriate for single amino acids or large biomolecules probe[35]. In contrast, tyrosine electrophilic iodination, as the most direct and widely applied approach, is simple, efficient, and reproducible, and was therefore more

suitable for this study. Despite its lower intrinsic stability relative to Bolton-Hunter labelling, the *in vitro* and *in vivo* stability assays in this study demonstrated sufficient stability for theranostic use. Furthermore, high apparent specific activity is crucial for the targeting ability of the probe. In our previous research, we reported that iodination of the polypeptide significantly alters its polarity, allowing for complete separation of the product from the unlabelled precursor by pre-HPLC[36]. Therefore, in this study, we incorporated tyrosine for iodine labelling and purified the product by pre-HPLC to obtain [^{131}I]I-Tyr-D-peptide-PEG$_{11}$-Tz, which has high apparent specific activity and improved click efficiency.

Biodistribution studies demonstrated that [^{131}I]I-Tyr-D-peptide-PEG$_{11}$-Tz was rapidly cleared from non-target organs over time while remaining relatively stable within tumors, which can be attributed to the multiple structural optimizations incorporated into the Tz design. The higher renal uptake observed is consistent with its predominant clearance pathway through the kidneys. Compared with [^{89}Zr]Zr-DFO-Per, which showed markedly higher uptake across most major organs and tumors, [^{131}I]I-Tyr-D-peptide-PEG$_{11}$-Tz achieved significantly lower off-target accumulation. Although its absolute tumor uptake was lower, the tumor-to-blood and tumor-to-liver ratios were superior, providing higher imaging contrast and more favorable dosimetric properties. These characteristics underscore the value of [^{131}I]I-Tyr-D-peptide-PEG$_{11}$-Tz in pretargeting strategies, where overall selectivity and safety outweigh absolute uptake values. Organ dosimetry analysis further demonstrated that radiation exposure to major normal tissues was within an acceptable range, with kidneys representing the primary dose-limiting organ, consistent with the renal clearance pathway of the small-molecule radioligand (Supporting Information Table S3). In this context, we also evaluated directly radioiodinated pertuzumab ([^{131}I]I-Per) as a potential therapeutic comparator. However, [^{131}I]I-Per exhibited limited *in vitro* radiochemical stability, with approximately 80% remaining at 12 h (Supporting Information Fig. S28). More importantly, partial *In vivo* deiodination led to loss of targeting capability and undesirable thyroid accumulation, while the intact fraction of [^{131}I]I-Per showed prolonged blood circulation. These properties are associated with increased risks of hematological toxicity and radiation exposure to highly perfused organs, raising safety concerns regarding its use in systemic radionuclide therapy studies. Consequently, [^{131}I]I-Per was not further pursued as a therapeutic comparator in this work, and the pretargeted strategy was instead designed to overcome these intrinsic limitations of directly radioiodinated IgG antibodies. Therapeutic studies further confirmed its efficacy, as the radiopharmaceutical exhibited prolonged retention within tumors, enabling effective tumor cell killing. In the high-dose group, tumor volumes at the study endpoint (Day 27) were markedly smaller compared with the low-dose and control groups, demonstrating promising therapeutic potential. In terms of safety, [^{131}I]I-Tyr-D-peptide-PEG$_{11}$-Tz benefited from rapid blood clearance, renal excretion, and reduced off-target radiation burden, collectively contributing to a favorable safety profile. Even at the higher administered dose, no significant toxicity was observed in blood analyses or H&E of major organs. This combination of selective tumor retention, therapeutic efficacy, and safety highlights the translational potential of this pretargeting system. From a conceptual perspective, this strategy is consistent with the emerging paradigm of nanoscale brachytherapy, which emphasizes highly localized radionuclide deposition within tumors to maximize therapeutic efficacy while minimizing systemic radiation exposure[37].

Radionuclide delivery system involving Per remain relatively underexplored, presenting further investigation opportunities. We selected pertuzumab as the lead molecule for the following reasons. First-line treatment for HER2-positive solid tumors (*e.g.*, breast cancer and gastric cancer) often involves trastuzumab. However, after high-dose trastuzumab therapy, the HER2 binding sites are typically blocked by trastuzumab. Studies have shown that Per binds to a different epitope on HER2 than trastuzumab does and that the binding of trastuzumab to HER2 does not interfere with Per binding[38]. Therefore, pretargeting therapy using Per is suitable for patients who have previously received trastuzumab treatment. Our pretargeting strategy using Per as the lead molecule may be more clinically translatable.

5. Conclusions

This study introduces a novel tetrazine probe within a HER2-targeted radionuclide delivery system, enabling selective iodine-131 delivery for integrated diagnosis and therapy, with promising potential for clinical translation.

Acknowledgments

This study was supported by the National Natural Science Foundation of China (82172002 and 82472037), Shanghai Rising-star Program (No. 22QA1408600, China) and the construction project of Shanghai Key Laboratory of Molecular Imaging (KFKT-2024-01, China) and the Youth Fund of Zhongshan Hospital, Fudan University (2024ZSQN03, China).

Authors contributions

All authors contributed to the study conception and design. Pengcheng Ma, Hui Tan and Qingyu Lin contributed equally to this work. Materials preparation, data collection, and analysis were performed by all authors. The first draft of the manuscript was written by Pengcheng Ma, Zonghua Luo, Dai Shi. and Dengfeng Cheng. All authors read and approved the final manuscript.

Conflicts of interest

The authors declare no conflicts of interests.

Supporting information

Supporting information to this article can be found online at https://doi.org/10.1016/j.apsb.2026.03.004.

References

1. Herrmann K, Schwaiger M, Lewis JS, Solomon SB, McNeil BJ, Baumann M, et al. Radiotheranostics: a roadmap for future development. *Lancet Oncol* 2020;**21**:e146−56.
2. Liu X, Song Y, Cheng P, Liang B, Xing D. Targeting HER2 in solid tumors: unveiling the structure and novel epitopes. *Cancer Treat Rev* 2024;**130**:102826.
3. Yoon J, Oh DY. HER2-targeted therapies beyond breast cancer — an update. *Nat Rev Clin Oncol* 2024;**21**:675−700.
4. Chen YF, Xu YY, Shao ZM, Yu KD. Resistance to antibody−drug conjugates in breast cancer: mechanisms and solutions. *Cancer Commun* 2023;**43**:297−337.

5. Meric-Bernstam F, Makker V, Oaknin A, Oh DY, Banerjee S, González-Martín A, et al. Efficacy and safety of trastuzumab deruxtecan in patients with HER2-expressing solid tumors: primary results from the DESTINY-PanTumor02 Phase II Trial. *J Clin Oncol* 2024;**42**:47−58.
6. Tamura K, Kurihara H, Yonemori K, Tsuda H, Suzuki J, Kono Y, et al. ^{64}Cu-DOTA-Trastuzumab PET imaging in patients with HER2-positive breast cancer. *J Nucl Med* 2013;**54**:1869−75.
7. Mortimer JE, Bading JR, Colcher DM, Conti PS, Frankel PH, Carroll MI, et al. Functional imaging of human epidermal growth factor receptor 2—positive metastatic breast cancer using ^{64}Cu-DOTA-Trastuzumab PET. *J Nucl Med* 2014;**55**:23−9.
8. Ulaner GA, Hyman DM, Ross DS, Corben A, Chandarlapaty S, Goldfarb S, et al. Detection of HER2-positive metastases in patients with HER2-negative primary breast cancer using ^{89}Zr-Trastuzumab PET/CT. *J Nucl Med* 2016;**57**:1523−8.
9. Gaykema SBM, Schröder CP, Vitfell-Rasmussen J, Chua S, Munnink THO, Brouwers AH, et al. 89Zr-trastuzumab and 89Zr-bevacizumab PET to evaluate the effect of the HSP90 inhibitor NVP-AUY922 in metastatic breast cancer patients. *Clin Cancer Res* 2014;**20**:3945−54.
10. Crow DM, Williams L, Colcher D, Wong JY, Raubitschek A, Shively JE. Combined radioimmunotherapy and chemotherapy of breast tumors with Y-90-labeled anti-Her2 and anti-CEA antibodies with Taxol. *Bioconjug Chem* 2005;**16**:1117−25.
11. Menon SR, Mitra A, Chakraborty A, Tawate M, Sahu S, Rakshit S, et al. Clinical dose preparation of [^{177}Lu]Lu-DOTA-Pertuzumab using medium specific activity [^{177}Lu]$LuCl_3$ for radioimmunotherapy of breast and epithelial ovarian cancers, with HER2 receptor over-expression. *Cancer Biother Radiopharm* 2022;**37**:384−402.
12. Kondo M, Cai Z, Chan C, Brown MK, Reilly RM. Preclinical comparison of [(111)In]In- and [^{225}Ac]Ac-DOTA-Trastuzumab IgG, $F(ab')_2$ and Fab for theranostic SPECT/CT imaging and α-Particle radioimmunotherapy of HER2-positive human breast cancer. *Mol Pharm* 2025;**22**:474−87.
13. Shi D, Fu W, Tan H, Lin Q, Shi H, Cheng D. Preclinical evaluation of 99mTc-MAG3-5-Fab targeting TREM2 in lung cancer mouse models: a comparison with 99mTc-MAG3-5-$F(ab')_2$. *Mol Pharm* 2024;**21**:303−12.
14. Sartor O, de Bono J, Chi KN, Fizazi K, Herrmann K, Rahbar K, et al. Lutetium-177-PSMA-617 for metastatic castration-resistant prostate cancer. *N Engl J Med* 2021;**385**:1091−103.
15. Chung YW, Kim S, Hong JH, Lee JK, Lee NW, Lee YS, et al. Overexpression of HER2/HER3 and clinical feature of ovarian cancer. *J Gynecol Oncol* 2019;**30**:e75.
16. Wolff AC, Somerfield MR, Dowsett M, Hammond MEH, Hayes DF, McShane LM, et al. Human epidermal growth factor receptor 2 testing in breast cancer: ASCO-College of American pathologists guideline update. *J Clin Oncol* 2023;**41**:3867−72.
17. Saxena A, Wu D. Advances in therapeutic Fc engineering-modulation of IgG-associated effector functions and serum half-life. *Front Immunol* 2016;**7**:580.
18. Song H, Xu M, Cai J, Chen J, Liu Y, Su Q, et al. ^{225}Ac-Labeled antibody for fibroblast activation protein-targeted alpha therapy. *Chem Biomed Imaging* 2023;**1**:628−36.
19. Grana C, Chinol M, Robertson C, Mazzetta C, Bartolomei M, De Cicco C, et al. Pretargeted adjuvant radioimmunotherapy with yttrium-90-biotin in malignant glioma patients: a pilot study. *Br J Cancer* 2002;**86**:207−12.
20. Kraeber-Bodéré F, Rousseau C, Bodet-Milin C, Frampas E, Faivre-Chauvet A, Rauscher A, et al. A pretargeting system for tumor PET imaging and radioimmunotherapy. *Front Pharmacol* 2015;**6**:54.
21. Sörensen J, Velikyan I, Sandberg D, Wennborg A, Feldwisch J, Tolmachev V, et al. Measuring HER2-receptor expression in metastatic breast cancer using [68Ga]ABY-025 affibody PET/CT. *Theranostics* 2016;**6**:262−71.
22. Zeglis BM, Sevak KK, Reiner T, Mohindra P, Carlin SD, Zanzonico P, et al. A pretargeted PET imaging strategy based on bioorthogonal diels-alder click chemistry. *J Nucl Med* 2013;**54**:1389−96.
23. Knight JC, Mosley M, Uyeda HT, Cong M, Fan F, Faulkner S, et al. *In vivo* pretargeted imaging of HER2 and TAG-72 expression using the HaloTag enzyme. *Mol Pharm* 2017;**14**:2307−13.
24. Oroujeni M, Tano H, Vorobyeva A, Liu Y, Vorontsova O, Xu T, et al. Affibody-mediated PNA-based pretargeted cotreatment improves survival of trastuzumab-treated mice bearing HER2-expressing xenografts. *J Nucl Med* 2022;**63**:1046−51.
25. Zeglis BM, Lewis JS. Click here for better chemistry. *N Engl J Med* 2022;**387**:2291−3.
26. Miao Y, Wang Y, Chen Y, Huang Z, Lu C, Liu Y, et al. Pretargeted multimodal tumor imaging by enzymatic self-immobilization labeling and bioorthogonal reaction. *J Am Chem Soc* 2025;**147**:2809−21.
27. Xenaki KT, Oliveira S, van Bergen En Henegouwen PMP. Antibody or antibody fragments: implications for molecular imaging and targeted therapy of solid tumors. *Front Immunol* 2017;**8**:1287.
28. Pyzik M, Sand KMK, Hubbard JJ, Andersen JT, Sandlie I, Blumberg RS. The neonatal Fc receptor (FcRn): a Misnomer?. *Front Immunol* 2019;**10**:1540.
29. Sims M, Kyriakou S, Matthews A, Deary ME, Kozhevnikov VN. Catching up with tetrazines: coordination of Re(I) to 1,2,4-triazine facilitates an inverse electron demand Diels-Alder reaction with strained alkynes to a greater extent than in corresponding 1,2,4,5-tetrazines. *Dalton Trans* 2023;**52**:10927−32.
30. Läppchen T, Rossin R, van Mourik TR, Gruntz G, Hoeben FJM, Versteegen RM, et al. DOTA-tetrazine probes with modified linkers for tumor pretargeting. *Nucl Med Biol* 2017;**55**:19−26.
31. Stéen EJL, Jørgensen JT, Denk C, Battisti UM, Nørregaard K, Edem PE, et al. Lipophilicity and click reactivity determine the performance of bioorthogonal tetrazine tools in pretargeted *in vivo* chemistry. *ACS Pharmacol Transl Sci* 2021;**4**:824−33.
32. Lin Q, Tan H, Lin Q, Si Z, Mao W, Wang T, et al. A pretargeted imaging strategy for immune checkpoint ligand PD-L1 expression in tumor based on bioorthogonal Diels-Alder click chemistry. *Mol Imag Biol* 2020;**22**:842−53.
33. Qiu L, Lin Q, Si Z, Tan H, Liu G, Zhou J, et al. A pretargeted imaging strategy for EGFR-positive colorectal carcinoma *via* modulation of Tz-radioligand pharmacokinetics. *Mol Imag Biol* 2021;**23**:38−51.
34. Zhang Y, Lin Q, Wang T, Shi D, Fu Z, Si Z, et al. Targeting infiltrating myeloid cells in gastric cancer using a pretargeted imaging strategy based on bio-orthogonal Diels−Alder click chemistry and comparison with 89Zr-labeled anti-CD11b positron emission tomography imaging. *Mol Pharm* 2022;**19**:246−57.
35. Rangger C, Haubner R. Radiolabelled peptides for positron emission tomography and endoradiotherapy in oncology. *Pharmaceuticals* 2020;**13**:22.
36. Yang T, Shi D, Lin Q, Shen H, Tan H, Liu Y, et al. Synthesis, screening, and evaluation of theranostic molecular CPCR4-based probe targeting CXCR4. *Mol Pharm* 2024;**21**:2415−24.
37. Ghosh S, Lee SJ, Hsu JC, Chakraborty S, Chakravarty R, Cai W. Cancer Brachytherapy at the nanoscale: an emerging paradigm. *Chem Biomed Imaging* 2024;**2**:4−26.
38. Keating GM. Pertuzumab: in the first-line treatment of HER2-positive metastatic breast cancer. *Drugs* 2012;**72**:353−60.